Journal of Rheology

RESEARCH ARTICLE | NOVEMBER 14 2024

Assimilation of linear viscoelastic measurements by joint inference of relaxation spectrum

Sachin Shanbhag ✉ ; Ralm G. Ricarte ; Dana Ezzeddine ; Daniel Barzycki

J. Rheol. 69, 1–14 (2025)
https://doi.org/10.1122/8.0000869

Assimilation of linear viscoelastic measurements by joint inference of relaxation spectrum

Sachin Shanbhag,[1,a)] Ralm G. Ricarte,[2,b)] Dana Ezzeddine,[2] and Daniel Barzycki[2]

[1]*Department of Scientific Computing, Florida State University, Tallahassee, Florida 32306*
[2]*Department of Chemical and Biomedical Engineering, Florida A&M University-Florida State University College of Engineering, Tallahassee, Florida 32310*

(Received 3 May 2024; final revision received 10 October 2024; published 14 November 2024)

Abstract

We develop a two-stage computational method to assimilate linear viscoelastic material functions (LMFs), viz., stress relaxation modulus, creep compliance, and the complex modulus, by inferring a consensus discrete relaxation spectrum (DRS) that simultaneously fits all three LMFs. In the first stage, the DRS corresponding to the different LMFs is deduced independently, before they are combined heuristically to generate an initial guess for the consensus DRS. In the second stage, this initial guess is refined using nonlinear least squares regression. The effectiveness of this method for data fusion and validation is demonstrated by analyzing experimental data collected on two different polymer melt systems. We also investigate the performance of the method when the timescales probed by the LMFs do not overlap, or are limited to 4–6 decades, as is typically the case for thermorheologically complex materials. To explore these questions, we generate synthetic datasets by obscuring information from one of the experimental datasets. We find that the computational protocol works quite well. As expected, the quality of the inferred DRS is marginally impaired because information is suppressed.© *2024 Published under an exclusive license by Society of Rheology.* https://doi.org/10.1122/8.0000869

I. INTRODUCTION

The three most common linear viscoelastic (LVE) tests are stress relaxation, creep, and small amplitude oscillatory shear (SAOS) experiments. Each of these LVE tests yields a LVE material function (LMF), which is a function of either time (t) or angular frequency (ω). Stress relaxation and creep experiments provide the time-dependent LMFs relaxation modulus $G(t)$ and creep compliance $J(t)$, respectively. SAOS experiments provide the complex modulus $G^*(\omega) = G'(\omega) + iG''(\omega)$, where $G'(\omega)$ and $G''(\omega)$ are the elastic and viscous moduli, respectively [1]. Formally, these LMFs are equivalent—*perfect* knowledge of any single LMF is sufficient to infer all other LMFs [2]. Unfortunately, the LMFs obtained from experiments or simulations are not perfect: they suffer from noise and other measurement artifacts and probe only a limited window of timescales or frequencies.

Thus, each LVE test offers an imperfect and limited view of underlying dynamics, like the parable of the blind man and the elephant [3]. In this work, it is helpful to think of the underlying relaxation spectrum (RS) as the metaphorical "elephant" or object of interest. The primary aim of this paper is to develop a computational protocol that uses mathematical relations between the LMFs and the RS (described in Sec. II A) to integrate the results of different LVE tests and provide a more reliable characterization of a material's linear rheology. This endeavor simultaneously serves two important goals: data *fusion* and *validation*.

1. *Data fusion*: Examples of data fusion, where different measurements are assimilated into master plots by appealing to universality, are quite familiar to rheologists [4–6]. Perhaps, the most ubiquitous example is time-temperature superposition (TTS) [7], where data collected from LVE tests conducted at different temperatures are shifted along the time and modulus axes and superposed. TTS can dramatically extend the dynamic range of timescales over which a material is probed.

   Integrating data from independent experiments or LVE tests is another form of data fusion [8–10]. Different LVE tests often have complementary strengths. For example, $J(t)$ and $G(t)$ measurements at short timescales may exhibit artifacts from sudden stress or strain jumps. However, $G^*(\omega)$ does not suffer from these limitations due to continuous deformation and is more reliable for probing short timescales. On the other hand, probing long timescales using $G(t)$ and $G^*(\omega)$ is inconvenient because the torque produced in the rheometer can fall below the threshold of instrument sensitivity [11]. Fortunately, $J(t)$ measurements are reliable in this regime [1,2,12].

   As demonstrated in this work, it is possible to combine TTS and data fusion of different LVE tests to further widen the dynamic range probed. However, it is well known that TTS fails for many technologically important materials such as polymer blends, block copolymers, covalent adaptable networks [13,14], and systems that undergo phase transitions or temperature-induced structural change [1,7].

[a)] Author to whom correspondence should be addressed; electronic mail: sshanbhag@fsu.edu

[b)] Electronic mail: rricarte@eng.famu.fsu.edu

For such materials integrating data from different LVE tests at a fixed temperature can become particularly important.

2. *Data validation*: The task of reconciling different LMFs is also helpful for *data validation*, which can identify and isolate potential inconsistencies in experimental measurements. Since different LMFs are manifestations of the same underlying RS, they are mathematically constrained. In particular, $G(t)$ and $J(t)$ are linked by the convolution relation [1,2,15],

$$t = \int_0^t J(t')\, G(t-t')\, dt' = \int_0^t G(t')\, J(t-t')\, dt', \quad t \geq 0, \quad (1)$$

from which it can be shown that $J(t)$ and $G(t)$ asymptotically share a reciprocal relationship, i.e.,

$$G(0)J(0) = G(\infty)J(\infty) = 1. \quad (2)$$

Similarly, the elastic and viscous moduli, $G'(\omega)$ and $G''(\omega)$, are constrained by Kramers–Kronig relations (KKRs) [16,17],

$$\begin{aligned} G'(\omega) - G_e &= -\frac{2\omega^2}{\pi}\int_0^\infty \frac{G''(u)/u}{u^2-\omega^2}du, \\ G''(\omega) &= \frac{2\omega}{\pi}\int_0^\infty \frac{G'(u)-G_0}{u^2-\omega^2}du, \end{aligned} \quad (3)$$

where $G_e = G'(\omega \to 0)$ is the equilibrium modulus or low-frequency plateau in the storage modulus. $G_e \neq 0$ for viscoelastic solids, and $G_e = 0$ for viscoelastic liquids. Potential violations of KKR may arise when mastercurves are created by the superposition of several independent datasets [18–20].

The extent to which experimentally obtained LMFs are consistent with each other can be assessed by the degree to which they obey or deviate from the convolution relation and KKR. A standard test to determine compliance of dynamic moduli with KKR is to infer an RS by simultaneously fitting a set of Maxwell modes to the storage and loss moduli [21–24]. Similarly, the consistency of $J(t)$ and $G(t)$ data with the convolution relation can be assessed by fitting a common RS to these two LMFs.

A. Strategy and layout

In this work, we seek a common RS that simultaneously describes all experimental observations. This representation is theoretically guaranteed to obey both KKR and the convolution relation, by design. Thus, it concurrently addresses the goals of data fusion and validation. While it is straightforward to integrate $G(t)$ and $G^*(\omega)$, incorporation of creep measurements is more challenging because $J(t)$ is naturally parameterized by a *retardation spectrum* (see Sec. II A), rather than an RS. Thus, assimilation of $J(t)$ requires methods for interconversion of compliance to modulus. Several numerical methods based on the convolution relation have been proposed [2,25–40], a subset of which is based on interconversion of retardation and RS [2,32–40]. Unlike methods that perform direct interconversion, we prefer methods based on RS because this choice closely aligns with the goal of this work which is to infer a common RS. Furthermore, these methods strictly obey both KKR and the convolution relation, which is not the case for methods based on numerical discretization for approximating derivatives or integrals. Recently, an efficient and robust computer program called PSI (for Prony series interconversion) that uses the convolution relation to convert a discrete retardation spectrum to a discrete RS and vice versa was developed [41]. This free and open-source program improves the stability of a method previously proposed by Loy *et al.* [40] by numerically bypassing potential singularities. The speed and robustness of PSI are instrumental in our ability to simultaneously fit different LMFs because it is required at every iteration during optimization to compute how well a candidate RS fits the observed $J(t)$ (see Sec. II C).

We begin by describing the mathematical relations that bind the different LMFs in Sec. II A. Experimental data in which all three LMFs are measured for the same material over a wide range of overlapping timescales are surprisingly limited. Therefore, we report LMFs for two different commercial polymers in Sec. II B. We use one of these datasets to illustrate the computational method developed here in Sec. II C. In this work, we equally weight the three LMFs to infer a common RS. This poses the risk of potentially contaminating high quality measurements with low quality ones. We attempt to mitigate this risk by standardizing experimentally measured LMFs so that they are of comparable quality (Sec. II C). If a common RS that fits the LMFs cannot be found, further investigation may be required to separate low and high-quality LMFs. If the appropriate statistical weight for each dataset or data point can be ascertained *a priori*, then the assumption of equal weighting used in this work can be relaxed. After demonstrating the effectiveness of the protocol in Sec. III, we explore how well this method performs when experimental data are limited in Sec. IV.

II. METHODS

We begin by recapitulating the mathematical formulae that relate the RS and LMFs. After that we describe the tests performed on two different commercial polymer melts: (1) polystyrene (PS) and (2) poly(4-methylstyrene) (P4MS). Finally, we outline the computational protocol used to integrate LVE functions using the PS dataset for illustration.

A. Mathematical relations

The relaxation modulus is related to the RS via

$$G(t) - G_e = \int_{-\infty}^{\infty} H(\tau)\, e^{-t/\tau} d\log\tau = \sum_{i=1}^{n} g_i\, e^{-t/\tau_i}, \quad (4)$$

where the first equality defines the continuous RS $H(\tau)$ via a Fredholdm integral equation of the first kind [42], and the second equality defines an equivalent n-mode Maxwell model or discrete RS (DRS) $H_n = \{g_i, \tau_i\}_{i=1}^n$.

It is well known that both these equalities lead to ill-posed problems because they violate at least one of the following three Hadamard conditions for well-posedness [42–44]: (i) existence (at least one solution), (ii) uniqueness (at most one solution), and (iii) stability (continuous dependence on data). In the case of $H(\tau)$, condition (iii) is violated. In the case of H_n, conditions (ii) and (iii) are both violated. Therefore, extraction of $H(\tau)$ or H_n leads to an ill-posed problem even though $H(\tau)$ is unique and H_n is not [44–46]. Regularization is a common strategy used to counter condition (iii) and stabilize the extraction of the RS. However, there is no universal strategy to determine the optimal type and amount of regularization to use. Different algorithms make different choices that lead to different RS. Furthermore, other factors such as finite time and frequency windows, noise, and other measurement artifacts ensure that $H(\tau)$, like H_n, is nonunique in practice.

Fortunately, nonuniqueness is immaterial for the goals of this work, viz., data validation and fusion. The existence of any common RS that fits the LMFs (it does not have to be unique) is sufficient to assert consistency with both the KKR and the convolution relation. Furthermore, a common DRS helps with extrapolation of LMFs and expanding the dynamic range of experiments. A common heuristic used to aid generalization and avoid overfitting is parsimony or *sparsity*, which is the idea that fewer Maxwell modes are preferable to more. Practically, the shapes of $H(\tau)$ and H_n are similar [21], and comparable physical insights can be gleaned from either RS. The choice of which RS to use is dictated by the application, e.g., the DRS is preferred for calibrating multimode constitutive models to LVE data [47].

The elastic and viscous moduli are related to the RS via

$$G'(\omega) - G_e = \int H(\tau)\frac{(\omega\tau)^2}{1+(\omega\tau)^2}\, d\log\tau = \sum_{i=1}^{n} g_i \frac{(\omega\tau)^2}{1+(\omega\tau)^2},$$
$$G''(\omega) = \int H(\tau)\frac{(\omega\tau)}{1+(\omega\tau)^2}\, d\log\tau = \sum_{i=1}^{n} g_i \frac{(\omega\tau)}{1+(\omega\tau)^2}. \tag{5}$$

Given an RS, $G(t)$ and $G^{*}(\omega)$ can be calculated using Eqs. (4) and (5). The inverse problem of extracting the RS from $G(t)$ or $G^{*}(\omega)$ is poorly conditioned and hence more difficult. Nevertheless, given its fundamental importance in linear rheology, a number of computer programs that appeal to parsimony or use some form of regularization have been developed. These include DISCRETE [48], pyReSpect [49–51], CONTIN [52], FTIKREG [53,54], NLREG [55,56], GENEREG [57], BayesRelax [58], IRIS [33], etc.

Creep compliance is related to the retardation spectra via

$$\begin{aligned} J(t) - J_e &= \eta_0^{-1} t - \int_{-\infty}^{\infty} L(\tau)\, e^{-t/\tau} d\log\tau \\ &= \eta_0^{-1} t - \sum_{k=1}^{n} j_k e^{-t/\lambda_k}, \end{aligned} \tag{6}$$

where $L(\tau)$ is the continuous retardation spectrum, and $L_n = \{j_k, \lambda_k\}_{k=1}^{n}$ is the discrete retardation spectrum. The inverse viscosity η_0^{-1} is zero for solids and nonzero for liquids. J_e is the common symbol used to denote the equilibrium compliance $J(t \to \infty)$ for solids and the steady-state compliance, $\lim_{t\to\infty} J(t) - \eta_0^{-1} t$ for liquids. Many of the computer programs used to extract $H(\tau)$ or H_n from $G(t)$ can be repurposed to extract the retardation spectrum from creep compliance. In this work, we use the program pyJt to extract L_n, J_e, and η_0^{-1} from $J(t)$.[1]

The convolution theorem links $J(t)$ and $G(t)$. Using it, $H(\tau)$ can be related to $L(\tau)$, J_e, and η_0^{-1} via [1],

$$H(\tau) = J_e - \eta_0^{-1}\tau + \int_{-\infty}^{\infty} \frac{L(s)}{\tau/s - 1}\, d\log s. \tag{7}$$

However, numerical integration of Eq. (7) is computationally challenging due to the singularity at $s = \tau$ in the integrand. Fortunately, if a parsimonious discrete retardation spectrum L_n with well-separated retardation times is available, it is empirically observed to suppress numerical instability, making it feasible to compute H_n from L_n [28,35,36,59–61]. The mathematical relations to obtain G_e and H_n from J_e, η_0^{-1}, and L_n, and vice versa, are explicitly described in [40] and [41], and implemented in the computer program PSI that is used in this work.

B. Materials and experimental methods

1. *Materials*

Polystyrene (PS, $M_n = 220$ kg/mol, $M_w = 354$ kg/mol, Đ = 1.6), poly(4-methylstyrene) (P4MS, $M_n = 60$ kg/mol, $M_w = 137$ kg/mol, Đ = 2.3), pentaerythritol tetrakis (3-(3,5-di-tert-butyl-4-hydroxyphenyl)propionate) (Irganox 1010), and dichloromethane (DCM) were purchased from Sigma-Aldrich. The sample preparation and rheology of PS were previously described in [11].

2. *Sample preparation of P4MS*

3 g of P4MS were mixed with 15 ml of a solution containing 0.03 g of Irganox 1010 dissolved in DCM and then stirred for 2 h. Excess solvent was removed under reduced pressure using rotary evaporation. The sample was then transferred to a scintillation vial and dried under reduced pressure at 50 °C for 18 h to yield 2.7 g of P4MS containing 1 wt. % Irganox 1010.

3. *Size exclusion chromatography (SEC)*

SEC of polymer samples was conducted using an Agilent-Wyatt combination triple-detection SEC instrument, which featured three successive Agilent PL-gel Mixed C columns (25 °C THF mobile phase). The instrument was equipped with an Agilent 1260 infinity series pump, degasser, autosampler, and thermostatted column chamber. The triple-detection unit included the following: a MiniDawn TREOS three-angle light scattering detector, Optilab TrEX

---

[1] S. Shanbhag, pyJt: A python program to extract the continuous and discrete retardation spectra from creep compliance measurements, https://github.com/shane5ul/pyJt (2023)

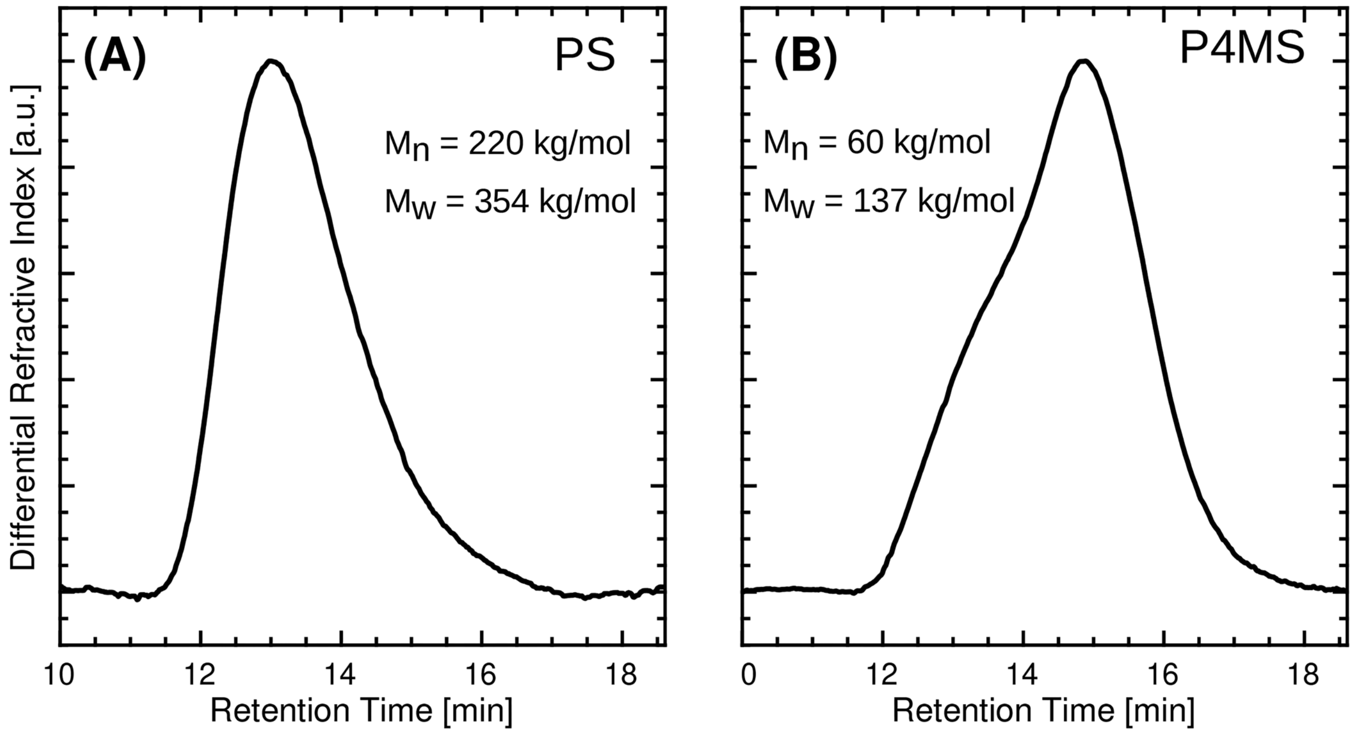

FIG. 1. SEC traces for the (a) PS (Đ = 1.6) and (b) P4MS (Đ = 2.3) samples.

refractive index detector, and a Viscostart II differential viscometer. SEC traces are shown in Fig. 1. To determine absolute molar masses, refractive index increments of 0.19 and 0.18 were used for PS and P4MS, respectively [62,63].

4. Rheology measurements

Linear viscoelasticity of P4MS was investigated using an Anton Paar MCR302e rotational rheometer with parallel plate geometry. The upper geometry was an aluminum disposable profiled plate (8 or 25 mm in diameter), while the lower geometry was a 25 mm stainless steel profiled plate with Peltier temperature control. Profiled surfaces were employed to reduce sample slip. The plate geometry was enclosed in a hood under a 200 l/h nitrogen flow to limit thermal degradation. The geometry achieved a temperature control accuracy of ±0.1 °C. During measurements, a normal force between 0.1N and 1N was applied to maintain contact between the sample and upper plate. P4MS samples were melt pressed into disk shapes (8 or 25 mm diameter, and 1 mm thickness) using stainless steel frames, with an applied load of 1 ton at 150 °C for 5 min.

Strain amplitude sweeps, small-amplitude oscillatory shear (SAOS), and creep measurements were conducted on the 8 mm diameter samples. Stress relaxation experiments were performed on both 8 and 25 mm diameter samples. Strain amplitude sweeps were conducted to identify the linear viscoelastic regime (LVE) at temperatures of 205 and 130 °C. For SAOS and stress relaxation, measurements on P4MS samples at all temperatures were performed at strain values within the LVE regimes identified at 205 and 130 °C. SAOS measurements were run at angular frequencies (ω) ranging from 100 to 0.01 rad/s. Stress relaxation and creep measurements were run for 0.5 h for temperatures ranging from 205 to 160 °C, 3 h at 145 °C, and 8 h at 130 °C. TTS was performed on SAOS, creep, and stress relaxation data using a reference temperature $T_R = 160\,^\circ\mathrm{C}$. Horizontal shift factors (a_T) were first applied to the SAOS tan δ versus ω plot to collapse the data into a continuous curve. Next, the horizontal shift factors were further refined by using the Williams–Landel–Ferry (WLF) equation

$$\log(a_T) = \frac{-C_1(T - T_R)}{C_2 + (T - T_R)}, \tag{8}$$

where C_1 and C_2 are empirical parameters. The horizontal shift factors determined using the WLF equation were applied to SAOS, stress relaxation, and creep data. Vertical shift factors (b_T) were determined by manually superposing the storage and loss moduli data of SAOS, stress relaxation, and creep. Results of TTS for PS and P4MS are shown in Figs. 2 and 3, respectively.

C. Computational protocol

The schematic diagram in Fig. 4 illustrates our overall approach for assimilating different LMFs by seeking a common RS. It proceeds in two stages. In the first stage, we use data collected from different LVE tests to *independently* infer the corresponding independent DRS and are denoted subsequently as iDRS. Subsequently, we attempt to heuristically merge the iDRS into a common spectra. Thus, the first stage provides an initial guess, H_n^0, for the joint spectrum. This is iteratively refined in the second stage using nonlinear least squares regression. During the jth iteration of the nonlinear regression, we compute the LMFs corresponding to a potential solution H_n^j. For $G(t)$ and $G^*(\omega)$, we use

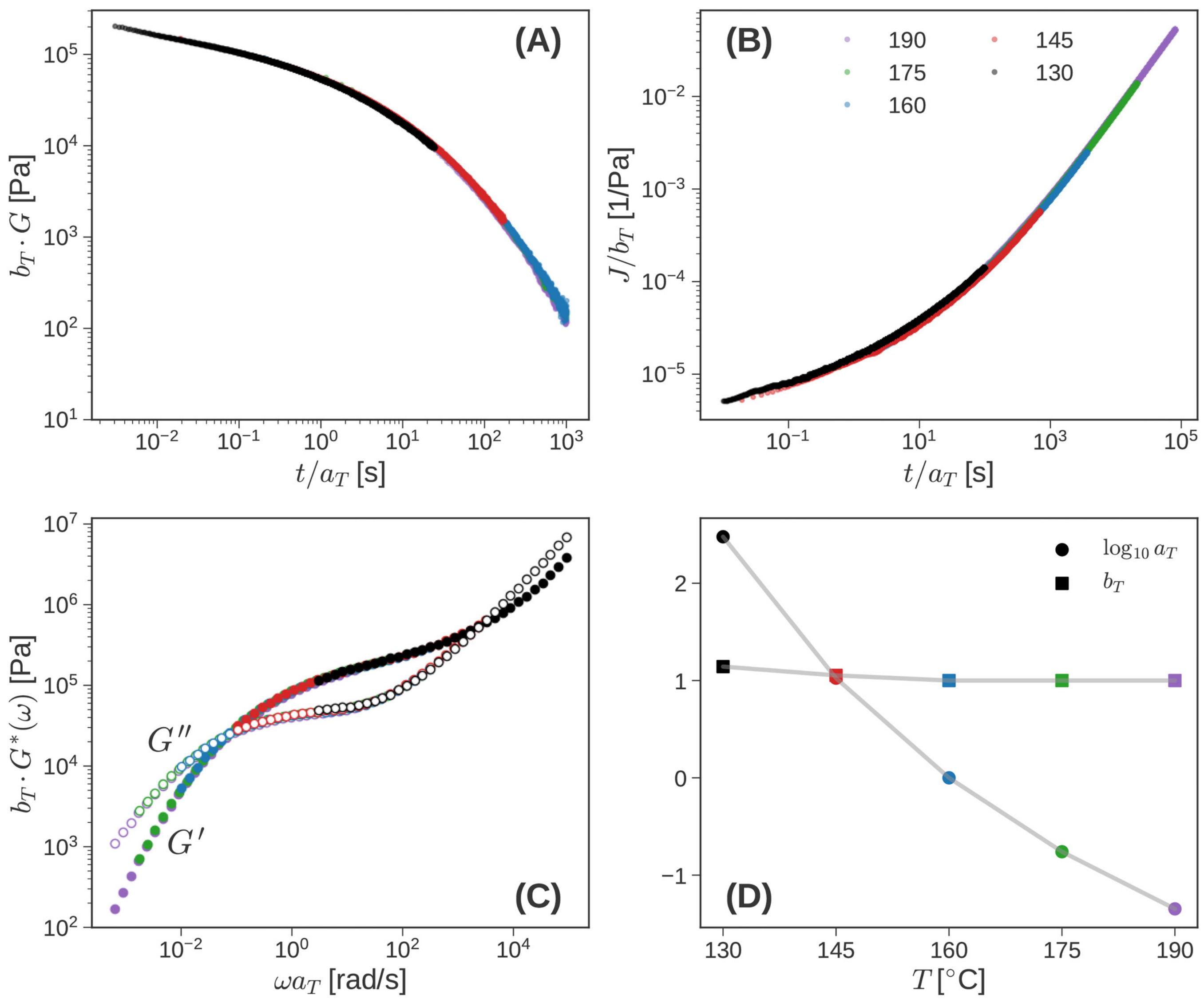

FIG. 2. TTS for PS using $T_{\text{ref}} = 160\,^{\circ}\text{C}$ as the reference temperature. A common set of shift factors (d) are used for superpose three different LMFs (a) stress relaxation, (b) creep compliance, and (c) complex modulus, where closed and open symbols denote $G'(\omega)$ and $G''(\omega)$, respectively.

Eq. (4) and (5), respectively. For $J(t)$, we first compute the retardation spectrum corresponding to H_n^j using PSI and then evaluate creep compliance using Eq. (6). We then use nonlinear regression to compare the predicted LMFs with the measured LMFs and iterate until convergence.

1. *Stage 1: Generating an initial guess*

It is helpful to present the details of the computational protocol with a concrete example. Therefore, we consider the PS dataset to animate the description. The posture we adopt in this work is to equally weigh the three measured LMFs (G, J, and G^*) and infer a common DRS from them. Therefore, raw data obtained from LVE tests have to be standardized and processed before they can be used to infer the RS to prevent contamination of high-quality signals by low quality signals.

The first few samples corresponding to short timescales collected during the measurement of $G(t)$ or $J(t)$ are unreliable due to inertial effects. Similarly, the signal in a stress relaxation measurement falls below instrument sensitivity at long times [11]. Therefore, for $G(t)$, we discard all data collected at times $t < 1$ s, with the knowledge that G^* is better at probing short timescales. We discard all long time $G(t)$ data after the relative error (noise-to-signal ratio) permanently exceeds 10%, with the knowledge that $J(t)$ offers a more reliable probe of this regime.

In addition to inertial effects, the $J(t)$ signal is weak at short times. Therefore, we use a more conservative threshold and discard all creep data collected at times $t < 3$ s. We do not trim long-time creep data or any of the SAOS data. The timescales interrogated by the different LMFs are visualized in Fig. 5(a) for PS, where the solid, dotted, and dashed lines represent $G(t)$, $J(t)$, and $G^*(\omega)$, respectively. The top panel shows how measurements at different temperatures extend the dynamic range of the timescales probed. The color scheme used to identify different temperatures in Fig. 5 is consistent with Figs. 2 and 3. Measurements at higher temperatures probe longer timescales.

The bottom panel compares the window of timescales examined by the three LMFs after TTS. For $G^*(\omega)$, the range

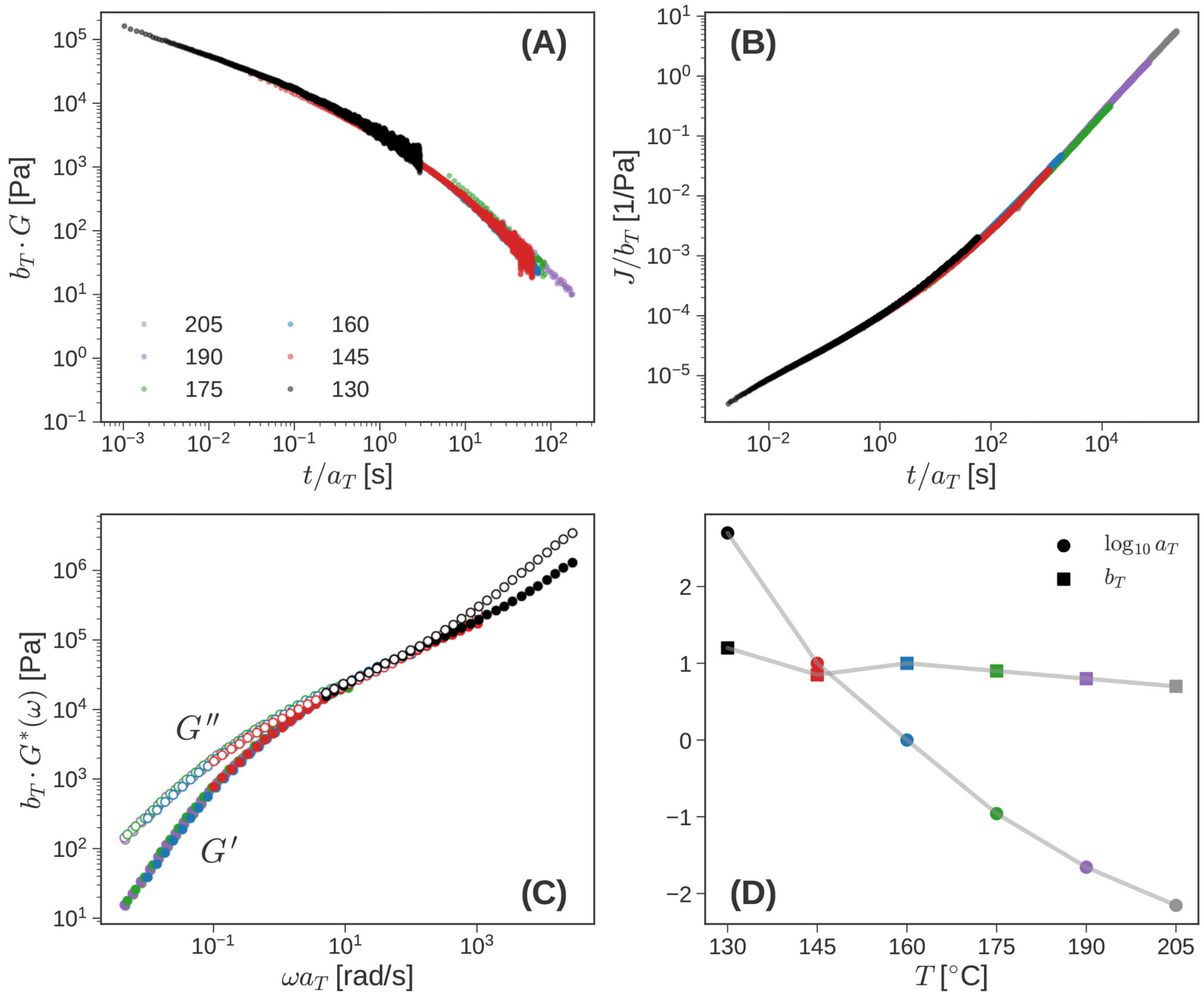

FIG. 3. TTS for P4MS using $T_{\mathrm{ref}} = 160\,°\mathrm{C}$ as the reference temperature. A common set of shift factors (d) are used for superpose three different LMFs (a) stress relaxation, (b) creep compliance, and (c) complex modulus, where closed and open symbols denote $G'(\omega)$ and $G''(\omega)$, respectively.

of timescales is identified as $[2\pi/\omega_{\max}, 2\pi/\omega_{\min}]$, where $\omega_{\min}$ and $\omega_{\max}$ are the minimum and maximum frequencies probed in Fig. 2(c), respectively. For PS, SAOS probes the shortest timescales $\sim 10^{-4}$ s, while creep accesses the longest timescales $\sim 10^5$ s, extending the overall range to approximately 9 decades. All three LMFs overlap over a broad range of intermediate timescales ($\sim 10^{-2}$–10^3 s) that spans nearly 5 decades. A qualitatively similar pattern is observed for P4MS in Fig. 5(b).

We down-sample the LMFs using linear interpolation on a logarithmically equispaced grid with $N = 100$ points. This is illustrated by blue crosses in Fig. 6. This transformation is motivated by two factors:

(i) Due to TTS, the density of data points in the mastercurves is nonuniform. Using raw data to infer a RS is equivalent to unintentionally weighing overlapping portions of the curves more strongly. If we believe that the mastercurves obtained from TTS approximate true material behavior, weighing different portions of the curve differently is unreasonable. Interpolation is required to weigh the mastercurve uniformly. In other words, interpolation is equivalent to unbiasing the arbitrary weights that result from TTS.

(ii) Using the same number of points ($N = 100$) to represent different LMFs equalizes the influence they have on the inferred cDRS. Otherwise, $J(t)$ [which has $\mathcal{O}(10^4)$ raw data points] is weighed approximately 100 times more strongly than SAOS [$\mathcal{O}(10^2)$ raw data points]. This is also computationally helpful because the cost scales with the number of observations.

These sanitized and interpolated data are subsequently used for computation of the spectra. Ultimately, the usefulness of the DRS inferred from these data can be ascertained by how well they describe the original raw data. Using this benchmark, the proposed protocol works satisfactorily as shown in Fig. 6.

We use the open source programs pyReSpect-time and pyReSpect-freq to independently infer the iDRS from $G(t)$

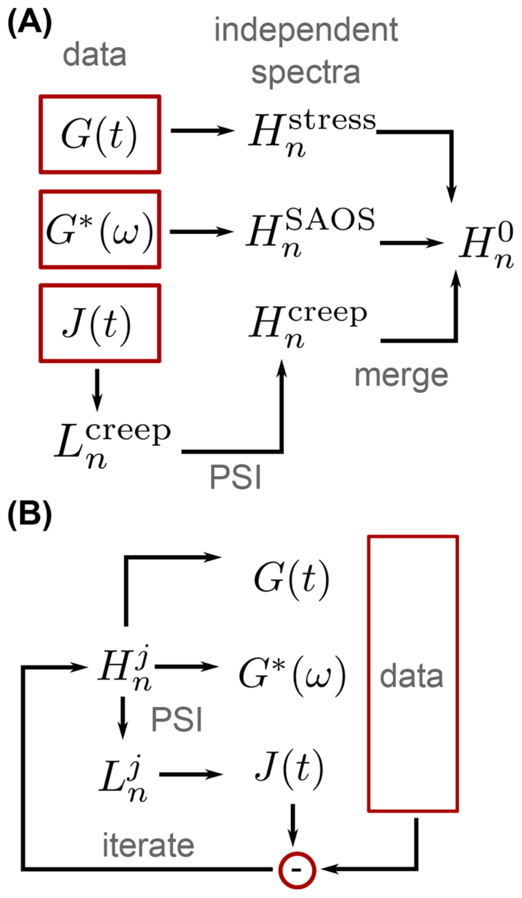

FIG. 4. Schematic diagram showing the two stages of the method used to infer the consensus DRS: (a) the DRS from different LMFs is independently computed and merged into an initial guess H_n^0; (b) this guess is refined until the least squares error is minimized.

and $G^*(\omega)$, respectively. pyReSpect uses a Bayesian criterion to determine the level of regularization required and performs nonlinear Tikhonov regression to infer the continuous RS. This informs the inference of a parsimonious DRS. The underlying methods are discussed in more detail in 50 and 51. We use pyJt to infer the discrete retardation spectrum L_n from $J(t)$. It is based on the same algorithm as pyReSpect and is also available for public download. We use PSI to convert the L_n to an iDRS. Fits obtained with the inferred iDRS are shown in Fig. 6.

The iDRS is shown in Fig. 7. The spectra obtained from $G(t)$, $G^*(\omega)$, and $J(t)$ have 10, 12, and 6 modes, respectively. In the region where they overlap, these iDRS have similar shapes. As expected, SAOS probes short timescales, while creep measurements probe long timescales. These data help to extend the range of timescales represented by the RS beyond the region where the iDRS overlap. The shortest relaxation time identified in Fig. 7 ($\sim 10^{-6}$ s), which originates from $G^*(\omega)$, is smaller than the shortest timescale probed by SAOS ($\sim 10^{-5}$ s) in Fig. 5(a). While some skepticism is warranted, it is not unusual for some of the relaxation times in a DRS to lie outside the window of timescales probed in an LVE test. Traces of a relaxation mode can persist for a decade or more, which allows us to detect and interpret them.

This claim can be crystallized using a simple example. Consider a hypothetical material that is well described using single mode Maxwell model with modulus G and relaxation time τ. The storage and loss moduli are given by $G'(\omega) = G\omega^2\tau^2/(1+\omega^2\tau^2)$ and $G''(\omega) = G\omega\tau/(1+\omega^2\tau^2)$, respectively. Suppose the relaxation time is long, and we are experimentally able to access only the large frequency

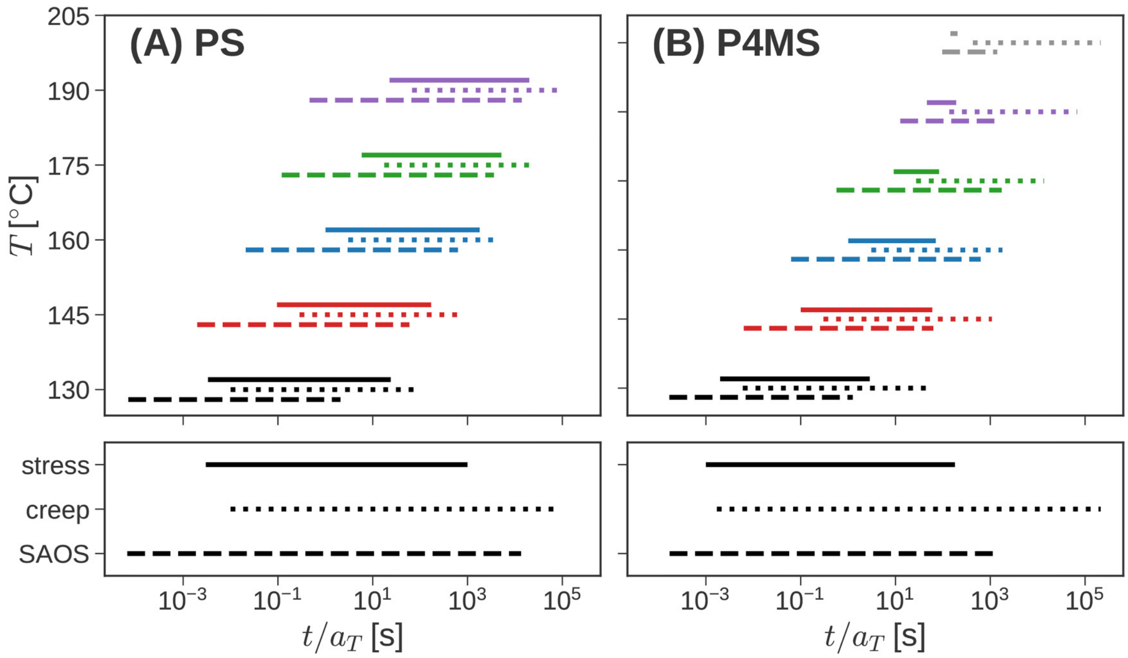

FIG. 5. The range of reliable timescales probed by different LVE experiments at different temperatures (top panels) for (a) PS and (b) P4MS. The reference temperature $T_{\text{ref}} = 160\,°\text{C}$. The overall ranges in Figs. 2(a)–2(c) and 3(a)–3(c) are shown in the bottom panels. Solid, dotted, and dashed lines represent the range of timescales probed by stress relaxation, creep, and SAOS experiments, respectively.

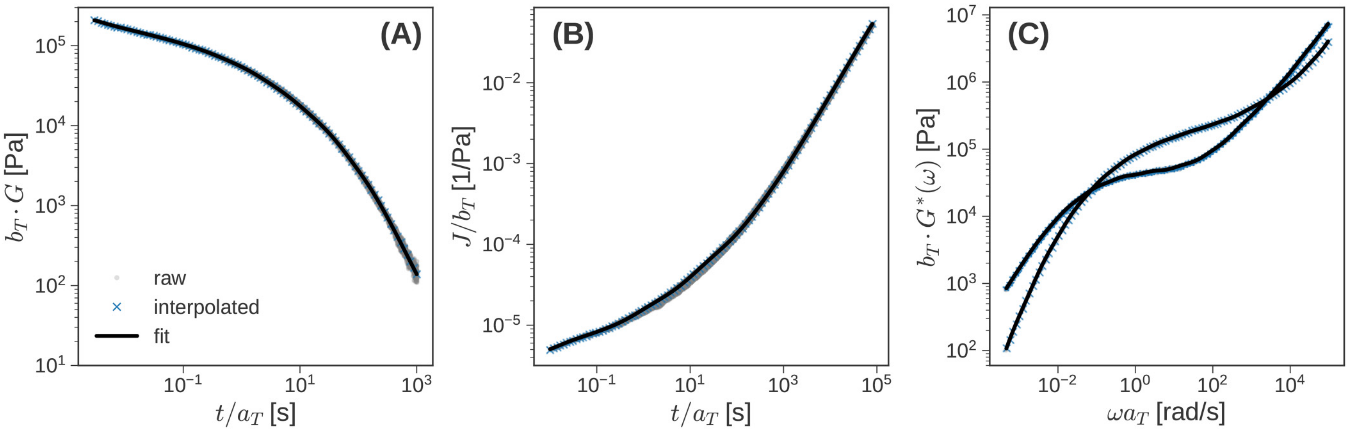

FIG. 6. A subset of the superposed raw data (gray symbols) from Fig. 2 is re-interpolated on a uniform time/frequency grid (blue crosses). Interpolated data are used *independently* to infer the discrete relaxation (a) and (c) and retardation (b) spectra from the moduli and creep measurements, respectively. The fits obtained from these spectra are shown using black lines.

response ($\omega \gg 1/\tau$) in a SAOS test. In this regime, $G'(\omega) \approx G$ is roughly constant, and $G''(\omega) \approx G(\omega\tau)^{-1}$ is inversely proportional to frequency. We can nonetheless estimate the location τ and strength G of the Maxwell mode, even though the range of frequencies does not straddle τ^{-1}.

After determining the three iDRS, we attempt to merge them into a single DRS. We start by considering the super-set of all the modes obtained, sort them according to relaxation time, and merge consecutive modes whose relaxation times differ by less than a factor of two. That is, when $\tau_{i+1}/\tau_i \leq 2$, we replace the two "old" modes with a single "new" mode that averages the two contributions. Specifically, we set

$$\tau_i^{\text{new}} = \frac{\tau_i^{\text{old}} + \tau_{i+1}^{\text{old}}}{2}, \qquad g_i^{\text{new}} = \frac{g_i^{\text{old}} + g_{i+1}^{\text{old}}}{2}, \qquad \tau_{i+1}^{\text{old}}/\tau_i^{\text{old}} \leq 2. \tag{9}$$

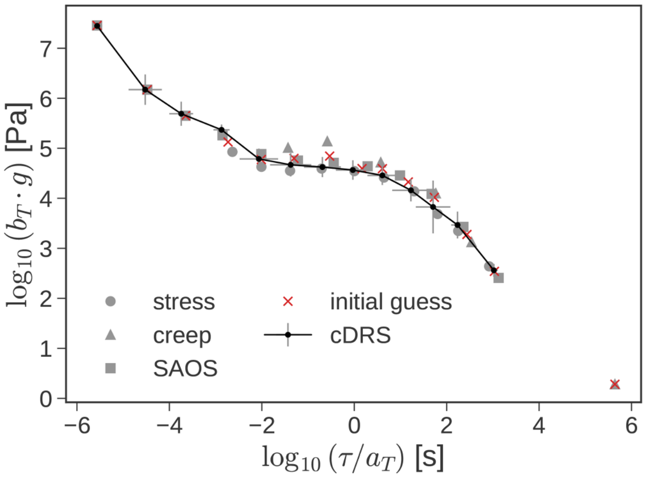

FIG. 7. The iDRS corresponding to $G(t)$ (circles), $J(t)$ (triangles), and $G^*(\omega)$ (squares) are shown by filled gray symbols. The initial guess (red crosses) for the common DRS is obtained by merging neighboring modes of the independent DRS. This initial guess is refined using nonlinear regression to simultaneously fit all the LMFs. The resulting cDRS (LSQ) is shown by black circles and connected by a line for clarity. Error bars are standard errors estimated from the covariance matrix estimated from the Jacobian matrix evaluated at the LSQ solution.

We recursively repeat this process of sorting and merging relaxation times, until no two relaxation timescales in the resulting spectrum are closer than a factor of two. This resulting initial guess, H_n^0, is shown by red crosses in Fig. 7. Starting from 28 initial modes between the RS corresponding to different LMFs, the resulting H_n^0 only has 14 modes. While H_n^0 depends on the order in which modes are merged (e.g., first to last, last to first, or closest to farthest), it does not matter in practice because H_n^0 only serves as an initial guess for the second stage.

2. *Stage 2: Nonlinear regression*

We denote experimental data with a "tilde," viz., $\left\{\tilde{t}_j^G, \tilde{G}_j\right\}_{j=1}^N$, $\left\{\tilde{t}_j^J, \tilde{J}_j\right\}_{j=1}^N$, and $\left\{\tilde{\omega}_j, \tilde{G}_j'\right\}_{j=1}^N$ and $\left\{\tilde{\omega}_j, \tilde{G}_j''\right\}_{j=1}^N$. Recall that we used $N = 100$ for all the LMFs when we interpolated the data on a uniform grid. This is not strictly required and may be relaxed, but it simplifies the following exposition. We pack the moduli and compliances into N dimensional vectors $\tilde{\boldsymbol{G}}$, $\tilde{\boldsymbol{J}}$, $\tilde{\boldsymbol{G}}'$, and $\tilde{\boldsymbol{G}}''$, so that the jth element of $\tilde{\boldsymbol{G}}$, for example, is $\tilde{G}_j$. Finally, we stack these vectors into a $4N$ dimensional *data vector* $\tilde{\boldsymbol{X}} = [\tilde{\boldsymbol{G}}, \tilde{\boldsymbol{J}}, \tilde{\boldsymbol{G}}', \tilde{\boldsymbol{G}}'']$.

During the computation, the DRS H_n is internally represented by a $2n$ dimensional vector $\boldsymbol{p} = [g_1, \ldots, g_n, \tau_1, \ldots, \tau_n]$ by concatenating the strengths and relaxation times. The stress relaxation modulus $G_j = G(\tilde{t}_j^G, \boldsymbol{p})$, and the elastic and loss moduli $G_j' = G'(\tilde{\omega}_j, \boldsymbol{p})$ and $G_j'' = G''(\tilde{\omega}_j, \boldsymbol{p})$ corresponding to the DRS are computed at the experimental times $(\tilde{t}_j^G)$ and frequencies $(\tilde{\omega}_j)$ using Eqs. (4) and (5), respectively. Similarly, the creep compliance corresponding to $\boldsymbol{p}$ is evaluated by first computing L_n using PSI. Then, $J_j = J(\tilde{t}_j^J)$ is calculated using Eq. (6). We stack these predicted moduli and compliances into vectors $\boldsymbol{G}$, $\boldsymbol{J}$, $\boldsymbol{G}'$, and $\boldsymbol{G}''$ and eventually into a $4N$ dimensional *prediction vector* $\boldsymbol{X}(H_n) = [\boldsymbol{G}, \boldsymbol{J}, \boldsymbol{G}', \boldsymbol{G}'']^T$.

We can define a residual vector $\boldsymbol{r}$ based on the relative difference between the prediction and corresponding data vectors as

$$\boldsymbol{r}_i = \frac{\boldsymbol{X}_i - \tilde{\boldsymbol{X}}_i}{\tilde{\boldsymbol{X}}_i}, \quad i = 1, 2, \ldots, 4N, \tag{10}$$

where the subscript i denotes to the ith element of a vector. We can then define the joint least squares (LSQs) cost function as the sum of squared residuals

$$\chi^2(\boldsymbol{p}) = \frac{1}{2}\sum_{i=1}^{4N} \boldsymbol{r}_i^2. \qquad (11)$$

We minimize the cost function χ^2 using the trust region reflective algorithm in SciPy's optimization library [64,65] with H_n^0 as the initial guess. This modified Newton method is suitable for constrained optimization and allows us to set lower bounds on the relaxation strengths and times. This is important since physically g_i and τ_i cannot be negative. The (i, j)th element of the $4N \times 2n$ Jacobian matrix $\boldsymbol{J}_{ij} = \partial \boldsymbol{r}_i / \partial \boldsymbol{p}_j$ is estimated numerically in the method. With a good initial guess H_n^0, convergence is swift.

During the minimization, the number of modes n is unchanged, but the location and strengths of the DRS change. Sometimes, after the optimization step converges, two neighboring modes move close to each other and may be subsumed into a single mode. Therefore, after minimizing χ^2, we sort the relaxation timescales $\{\tau_i\}$ again and attempt to merge neighboring modes that are less than a factor of two apart. The motivation for dispersing relaxation modes is to (i) improve the numerical conditioning of the interconversion problem and (ii) impose parsimony, the most common heuristic used to deal with the nonuniqueness of the DRS. Small changes to this threshold (1.5–3) do not change results significantly, although it may be possible to improve the spacing of relaxation modes using a more systematic approach [66]. Using a factor of two as the threshold still allows for a reasonably high density of modes in the DRS. For context, even continuous $H(\tau)$ are typically resolved with $\sim$10 modes per decade, such that the spacing of neighboring modes is $10^{1/10} \approx 1.26$. Since the solution is perturbed by this operation, the minimization step is repeated with the perturbed DRS as the initial guess. This sequence of minimization and merger of nearby modes is repeated until all the relaxation times are separated by a factor greater than two. This optimal solution H_n^* is labeled "cDRS" (for *consensus* or *common* DRS) in Fig. 7.

For the PS dataset, two cycles of minimization were required. The first minimization, $H_n^{(1)}$ required 18 iterations and 36 function evaluations. This implies that PSI was called 36 times during the optimization process. Two modes that drifted close were subsumed, and the number of modes decreased from 14 to 13. A second minimization step with 21 iterations and 23 function evaluations was required to refine this solution and obtain the final LSQ solution $\boldsymbol{p}_*$ corresponding to $H_n^* = H_n^{(2)}$. This entire process took less than 10 s on an old 2.3 GHz Intel Xeon CPU.

The uncertainty in the estimated solution is estimated by linearizing χ^2 near the LSQ solution to obtain the covariance matrix of the estimated parameters $\boldsymbol{p}_*$ as

$$\mathrm{cov}(\boldsymbol{p}_*) = \frac{\chi^2(\mathrm{p}_*)}{4\mathrm{N} - 2\mathrm{n}} \left(\boldsymbol{J}_*^{\mathrm{T}} \boldsymbol{J}_*\right)^{-1} \qquad (12)$$

where $\boldsymbol{J}_*$ is the Jacobian matrix evaluated at the LSQ solution $\boldsymbol{p}_*$. The error bars shown in the Fig. 7 are standard deviations determined by taking the square-roots of the diagonal elements of this covariance matrix. It is useful to point out that the these error bars depict the uncertainty in model parameters and primarily reflect the nonuniqueness of the DRS rather than the mismatch between observations and the multimode Maxwell model.

III. RESULTS

We present results on the inference of the cDRS for the PS and P4MS samples in this section. Partial analysis of the PS sample was already presented in illustrating the algorithm for computing the cDRS. In the subsequent "Discussion" section, we re-analyze the PS data in a different way to get some insight into how this computational technique might generalize.

A. PS

Figure 8 shows how well the cDRS estimated for the PS sample fits experimental observations (symbols). The dashed red lines depict the predictions using H_n^0, the initial guess, which is shown by red crosses in Fig. 7. Even the initial

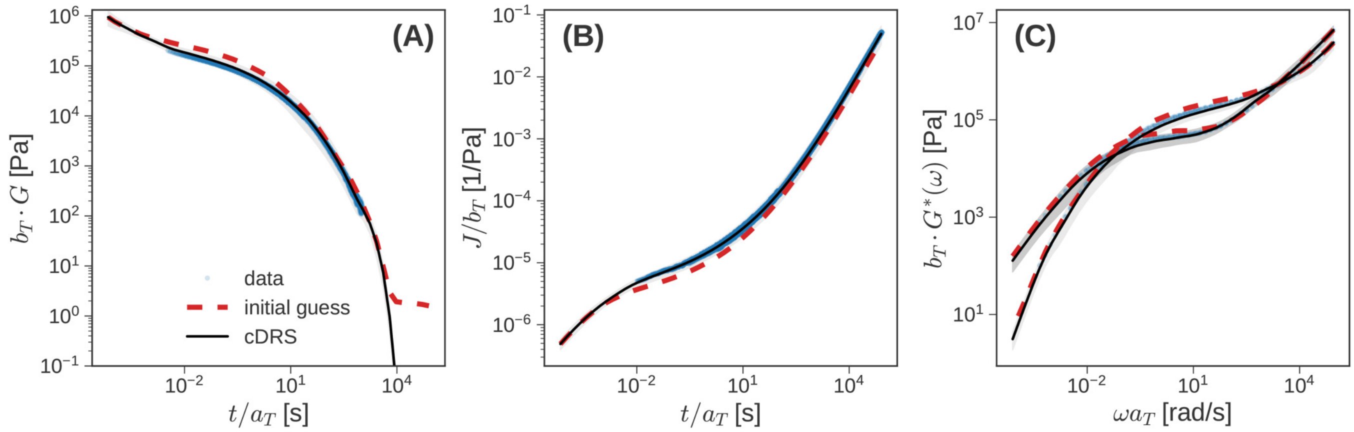

FIG. 8. Fits to the LVE data (symbols) obtained using the initially guessed RS (dashed red lines) and the optimal DRS obtained using nonlinear regression (solid black line). The shaded uncertainty band is estimated using Monte Carlo simulation as described in the text.

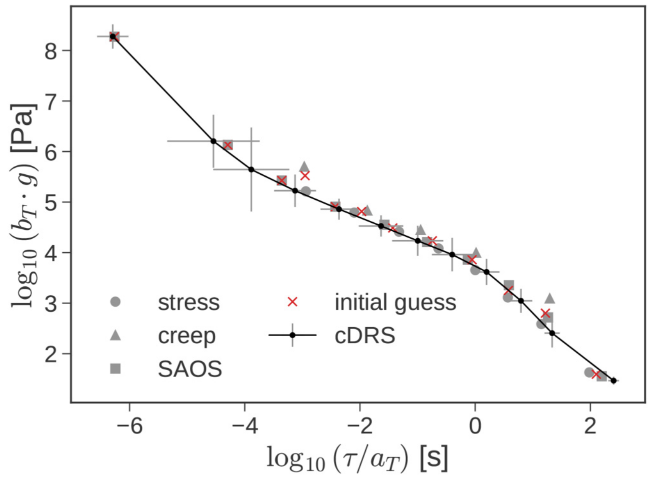

FIG. 9. Independent, initial guess, and consensus DRS for P4MS. The symbols and lines have meanings identical to Fig. 7.

guess does an acceptable job of simultaneously describing the three LMFs, especially over the range of the experimental data. Upon close inspection, it slightly overpredicts $G(t)$ and $G''(\omega)$ and underpredicts $J(t)$ over intermediate timescales. These deviations are correlated: overestimation of $G(t)$ necessarily leads to underestimation of $J(t)$ because of the convolution relation.

The black lines depict the predictions using the cDRS over the entire range of timescales [Fig. 5(a)] spanned by the LVE data. These predictions fix the slight over/under prediction obtained using H_n^0. Additionally, the mode corresponding to the longest relaxation time in H_n^0 is discarded in the cDRS. This corrects a spurious long-time shoulder observed in the $G(t)$ prediction using the initial guess. The relative error between the experimental and estimated LMFs can be quantified by the mean absolute value of the residual vector [Eq. (10)], which is of order ~0.1 (see the supplementary material). We perform Monte Carlo simulations (MCSs) to estimate the prediction error of the LSQ solution, which is shown by the gray shaded regions in Fig. 8. These uncertainty bands are estimated from 100 independent samples of the DRS drawn from a multidimensional Gaussian distribution with mean $\boldsymbol{p}_*$ and covariance given by Eq. (12). The standard error of the predicted LMFs is used to compute the width of the uncertainty band. Note that this estimate, with relative error of order ~0.3, accounts for the uncertainty in the fitted parameters.

B. P4MS

From Fig. 3, it is evident that the quality of TTS for the P4MS dataset is noisier than that of the PS dataset. Nevertheless, the computational protocol developed to compute a cDRS works reasonably well. Figure 9 shows the iDRS corresponding to the different LMFs, the initial guess after merging nearby modes and the cDRS obtained by fitting the LMFs simultaneously.

The iDRS corresponding to stress relaxation, creep, and SAOS data contained 8, 5, and 10 modes, respectively, for a total of 23 modes. After merging neighboring modes, this number was reduced to 12. Estimating the cDRS required 12 iterations and 23 function evaluations. The final number of modes remained unchanged at 12. As before, the entire process, which involved repeated calls to PSI, required only a few seconds on a single CPU.

Figure 10 compares the predictions of H_n^0 and H_n^*. The agreement of the cDRS predictions and the LVE data appears reasonable. The slowest relaxation mode (Fig. 9) near $\tau \approx 100\,\mathrm{s}$ results in a discernible shoulder in $G(t)$ at long times, and a noticeable change of slope in $G'(\omega)$ at low frequencies. Is this mode real or spurious?

From Fig. 5(b), the timescales probed by SAOS and creep experiments extend to approximately 10^3 and 10^5 s, respectively. Thus, we suspect that there is some signal in the observations that informs the presence of a small fraction of polymers that relaxes slowly. Indeed, the shoulder observed in the SEC trace in Fig. 1(b) indicates the presence of a high-molecular weight tail. The slopes of the observed $G'(\omega)$ and $G''(\omega)$ curves in Fig. 10 are not yet terminal, lending further support to the idea of a high molecular weight tail. Interestingly, the origin of this mode can be traced to the iDRS corresponding to $G^*(\omega)$ [and $G(t)$], and not $J(t)$ which becomes nearly terminal at large t, i.e., $J(t) \propto t$. On balance, we surmise that the longest relaxation mode identified is real,

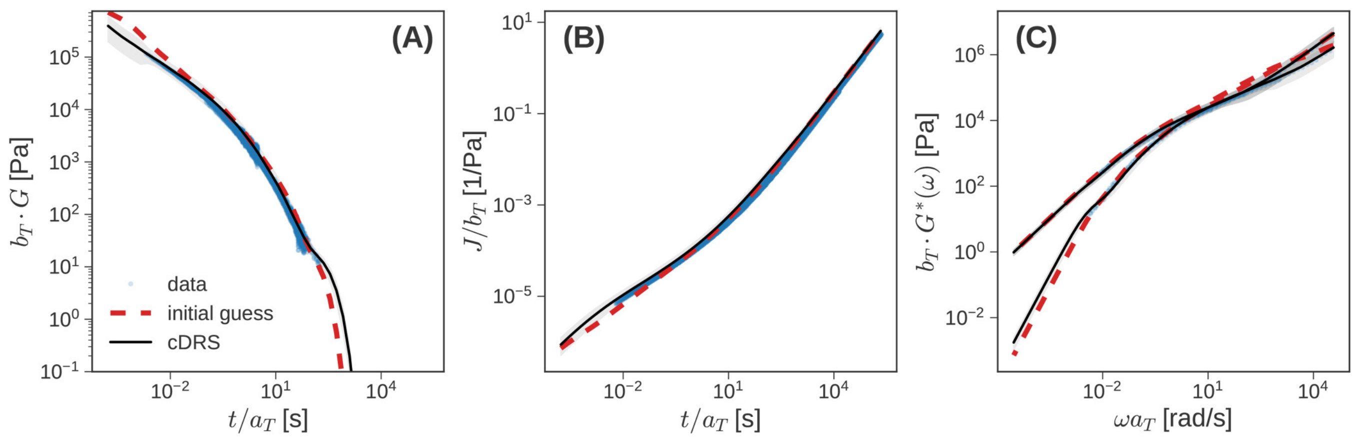

FIG. 10. Fits to the P4MS LVE data using H_n^0 and H_n^*. Symbols and lines have meanings identical to Fig. 8.

although there may be some doubt surrounding its precise location and strength.

IV. DISCUSSION

We invoked the metaphor of the blind men and the elephant in the introduction to motivate this work. However, it is clear from Fig. 5 that the timescales probed by different LMFs overlap over several orders of magnitude, leading to sharing of information. It is interesting to ask what happens when this is not the case. How much worse does the cDRS inferred from LMFs that probe nonoverlapping timescales get? We probe this question in Sec. IV A. This situation is qualitatively closer to the metaphor of the blind men and the elephant, since data are scarce and inference of the cDRS has to rely on the mathematical relationships that bind different LMFs.

A separate issue worth investigating is the applicability of the method to thermorheologically complex materials. Since PS and P4MS were thermorheologically simple, TTS was applied before the cDRS was inferred in results presented thus far. For thermorheologically complex materials, the cDRS has to be inferred from LMFs obtained at a fixed temperature. Generally, the range of timescales probed by standard LVE tests at a fixed temperature only span 4–6 decades, with SAOS and creep tests providing exclusive information at short and long timescales, respectively. It is well established that the inferred RS are least reliable near the ends of the domain [67]. Therefore, in Sec. IV B, we evaluate how the cDRS obtained at fixed temperatures compares with the original.

In both these scenarios, complete information is obscured either by revealing only portions of the observations (nonoverlapping timescales), or by concealing the applicability of TTS. Thus, we anticipate that the quality of the cDRS obtained in both these scenarios to worsen. We use the PS dataset to investigate both these questions. Qualitatively similar results are obtained using the P4MS dataset.

A. LMFs with nonoverlapping timescales

We generate a synthetic dataset with nonoverlapping timescales by cropping the LMFs from the original PS dataset. As shown in Fig. 5(a), the time intervals (in seconds) probed by SAOS, stress relaxation, and creep experiments that were used for inferring iDRS were $[6 \times 10^{-5}, 1.2 \times 10^{3}]$, $[5 \times 10^{-3}, 10^{3}]$, and $[10^{-2}, 8 \times 10^{4}]$, respectively. These are reproduced at the top of Fig. 11 for context. SAOS (dashed line) probes the shortest timescales, while creep probes the longest timescales. There is a broad intermediate region of about 5 decades where all three LMFs overlap. The cDRS inferred from this data, previously shown in Fig. 7, is reproduced and labeled “full” because it uses all available data for inference.

We then cropped the experimental data and retained only the subintervals $[6 \times 10^{-5}, 6 \times 10^{-1}]$, $[10^{1}, 10^{2}]$, and $[10^{3}, 8 \times 10^{4}]$ s from the original SAOS, stress relaxation, and creep measurements, respectively. These timescales are visualized at the bottom of Fig. 11. Thus, there are two “holes” of missing data, [0.6, 10] s and $[10^{2}, 10^{3}]$ s in these synthetically altered datasets. Furthermore, in contrast to the full data, there are no overlapping timescales in this partial dataset. Nevertheless, we can apply the computational protocol, and infer the cDRS shown in Fig. 11.

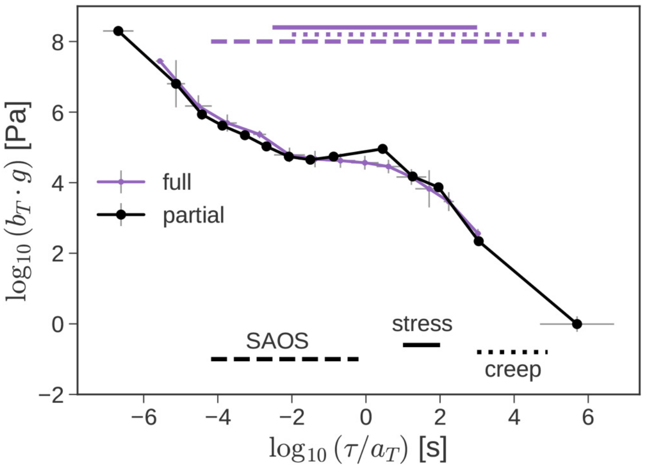

FIG. 11. The consensus DRS obtained using the full (purple dots) and partial (black circles) PS LVE datasets. The timescales probed by the LMFs for the full and partial datasets used to infer the DRS are shown at the top (purple), and bottom, respectively. Dashed, solid, and dotted lines show the reliable intervals spanned by SAOS, stress relaxation, and creep tests, respectively.

The cDRS obtained from the partial nonoverlapping data shows remarkable agreement with the cDRS inferred from the full dataset. Visually, the most conspicuous deviations between the two cDRS are observed near $\tau = 1$ and 10^{6} s. The fact that one of these mismatches ($\tau = 1$ s) occurs in one of the holes in the partial data is not a coincidence. Furthermore, the slower mode near $\tau = 10^{6}$ s is also visible in the iDRS obtained from creep observations in Fig. 7. In the full dataset, SAOS measurements inform the removal of this mode in the cDRS. However, it persists in the cDRS obtained from the partial dataset because neither SAOS nor stress relaxation experiments can dispute its placement. Nevertheless, the absence of overlapping LMFs does not present an insurmountable obstacle for the proposed computational protocol.

This is further corroborated in Fig. 12, which compares fits to experimental observations using the cDRS from the partial dataset. It should be stressed that only the data between the dashed blue lines were used for inferring the iDRS and hence the cDRS. This is clear from the nearly perfect fits to the data in these narrow regions. While the agreement outside these slices is far from perfect, it is still rather impressive. It is a manifestation of the transfer of information learned from fitting other LMFs. Even though the fits in Fig. 12 do not look as good as those in Figs. 8 and 10, it perhaps more remarkable in light of the scarce information used to obtain them.

B. Thermorheological complexity

In order to simulate the impact of thermorheological complexity on the inferred cDRS, we re-analyzed the PS data at different temperatures in a different order. Instead of performing TTS to obtain the superposed plots and shift factors

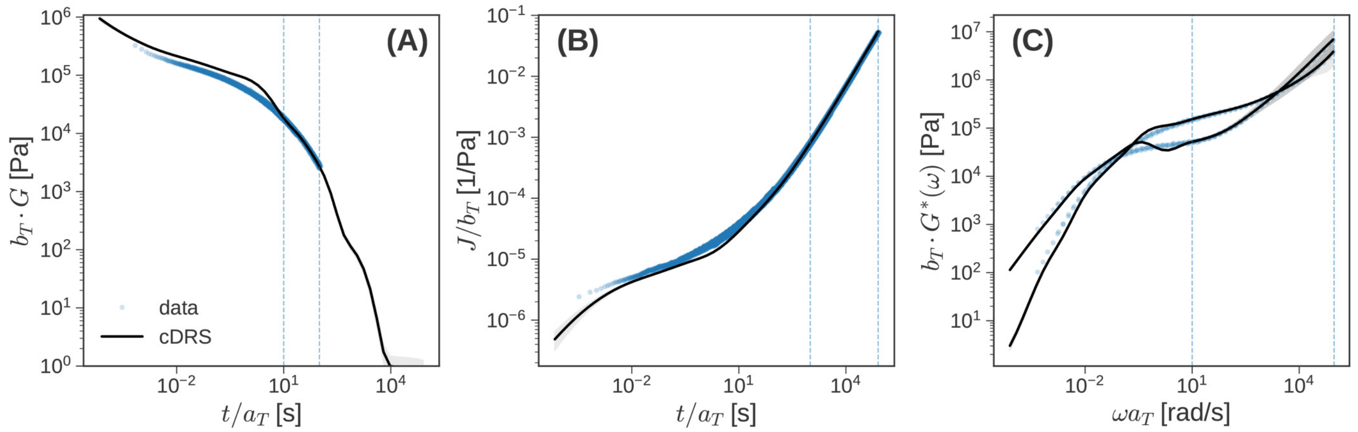

FIG. 12. Fits to the partial PS LVE data with nonoverlapping LMF timescales. Only the (partial) data between the dashed blue lines was used to infer the cDRS shown in Fig. 11.

shown in Fig. 2 before inferring the cDRS, we *independently* considered the raw LMFs obtained at the five different temperatures between 130 and 190 °C. The timescales spanned by the LMFs at different temperatures are depicted in the top panel of Fig. 5(a). Lower temperatures explore shorter timescales, while higher temperatures speed up dynamics, and allow us to probe longer timescales. At a particular temperature T, all the three LMFs ($G(t)$, $J(t)$, and $G^*(\omega)$) were used to obtain the cDRS $H_n^*(T)$ at that temperature. These $H_n^*(T)$ are shown in Fig. 13. These DRS are shifted using the shift factors shown in Fig. 2(d), so that they can be easily compared with each other, and the original cDRS that used superposed data.

We observe three features:

(i) The core of the cDRS inferred at different temperatures coincides with the core of the original cDRS, as expected. This provides some confidence that $H_n^*(T)$ can be reliably extracted from datasets that span a smaller window of timescales. This bodes well for applying this technique to thermorheologically complex materials.

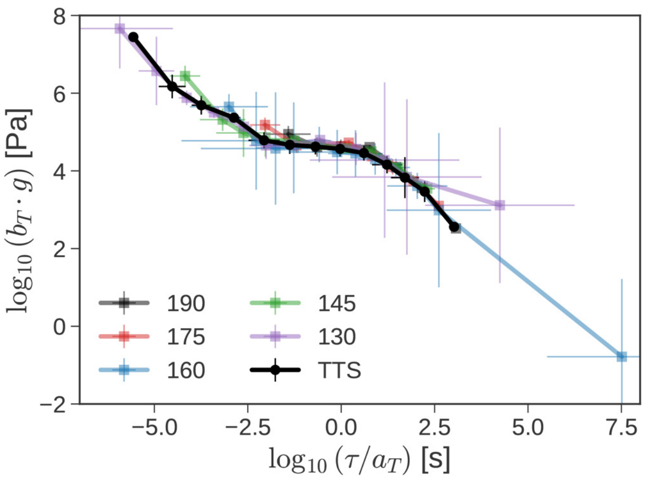

FIG. 13. Best-fit consensus DRS for PS obtained using only data at a particular temperature shifted to $T_{\text{ref}} = 160$ °C are shown by lines of different colors. The solid black line is the cDRS previously shown in Fig. 7 that used superposed data.

(ii) However, the modes at the ends of the cDRS inferred at different temperatures are characterized by large uncertainty. This uncertainty in the DRS modes is induced by finite-size effects. The slow relaxation modes in $H_n^*(T)$ for T = 130 and 160 °C are particularly noisy and unreliable. A practical implication of this observation is that for materials that obey TTS, it is better to perform TTS before assimilating different LMFs.

(iii) For most temperatures, the fastest relaxation mode in $H_n^*(T)$ seems to lie above the black line. This anomalous upturn in the DRS is a well-understood phenomenon. It arises because the first mode in $H_n^*(T)$ at a particular temperature attempts to capture the (attenuated) effect of all the modes in the full cDRS (black line) corresponding to faster timescales; i.e., those that lie to its left.

To summarize, the proposed method can be applied to all materials regardless of whether they obey TTS. However, for materials that obey TTS, it is better to superpose the LMFs before inferring the cDRS.

V. SUMMARY AND CONCLUSIONS

We proposed a computational method for assimilation of different LVE measurements by inferring a common DRS. This simultaneously meets the goals of data fusion, which extends or fills gaps in the dynamic range of timescales probed, and data validation, which automatically tests the consistency of the LMFs with the convolution and KKRs. We demonstrated the effectiveness of this protocol performing experiments and analyzing the LMFs on two different polymer melt systems (PS and P4MS).

The proposed method proceeds in two stages. In the first stage, the LMFs are analyzed independently to infer the respective iDRS. This operation used three open-source programs: we used PYRESPECT to infer iDRS from $G(t)$ and $G^*(\omega)$, while we used PYJT to first obtain the discrete retardation spectrum from $J(t)$ and then used PSI to convert this to a DRS. At the end of the first stage, we heuristically combined these independent DRS into an initial guess for the common DRS. In the second stage, we used nonlinear least squares regression to refine this initial guess. The cDRS inferred from both datasets fits experimental observations remarkably well. For the P4MS dataset, the analysis suggests the possibility of a high-molecular weight tail that prevents $G^*(\omega)$ from becoming terminal.

We also investigated the applicability of the method to data in which the timescales probed by the LMFs are nonoverlapping and to thermorheologically complex materials. The method works as expected, although the quality of the inferred cDRS deteriorate because information is suppressed. Nevertheless, we clearly see the merits of data fusion and transfer learning for nonoverlapping LMFs and the applicability of the method to thermorheologically complex materials where the range of timescales probed typically spans only 4–6 decades.

SUPPLEMENTARY MATERIAL

See the supplementary material for plots of the relative error between the experimental and estimated LMFs corresponding to Fig. 8.

ACKNOWLEDGMENTS

This work was partially supported by the National Science Foundation under Grant Nos. DMR-2144007 and DMR-1727870. The authors are very grateful to Dr. Justin Kennemur and the Kennemur Laboratory for use of their size-exclusion chromatography instrument. This work was partially supported by funds provided by the Oak Ridge Associated Universities Foundation, ORAU-Directed Research and Development Program. This work was partially supported by funds provided by the 3M Non-Tenured Faculty Award.

AUTHOR DECLARATIONS

Conflict of Interest

The authors have no conflicts to disclose.

DATA AVAILABILITY

Python code for the programs used is openly available in GitHub at https://github.com/shane5ul/. Other data that support the findings of this study are available from the corresponding author upon reasonable request.

REFERENCES

[1] Ferry, J. D., *Viscoelastic Properties of Polymers*, 3rd ed. (Wiley, New York, 1980).

[2] Tschoegl, N. W., *The Phenomenological Theory of Linear Viscoelastic Behavior: An Introduction*, 1st ed. (Springer, Munich, 1989).

[3] Saxe, J., and P. Galdone, *The Blind Men and the Elephant* (Whittlesey House, New York, 1963).

[4] Berry, G. C., and T. G. Fox, "The viscosity of polymers and their concentrated solutions," Adv. Polym. Sci. **5**, 261–357 (1968).

[5] Markovitz, H., "Superposition in rheology," J. Polym. Sci.: Polym. Symp. **50**, 431–456 (1975).

[6] Heo, Y., and R. G. Larson, "Universal scaling of linear and nonlinear rheological properties of semidilute and concentrated polymer solutions," Macromolecules **41**, 8903–8915 (2008).

[7] Dealy, J., and D. Plazek, "Time-temperature superposition—A users guide," Rheol. Bull **78**, 16–31 (2009).

[8] Talebi, S., R. Duchateau, S. Rastogi, J. Kaschta, G. W. M. Peters, and P. J. Lemstra, "Molar mass and molecular weight distribution determination of UHMWPE synthesized using a living homogeneous catalyst," Macromolecules **43**, 2780–2788 (2010).

[9] Shanbhag, S., "Inference of polymer structure by simultaneous analysis of chromatographic and rheological measurements," Rheol. Acta **52**, 973–988 (2013).

[10] Reyes, P., M. Edeleva, D. R. D'hooge, L. Cardon, and P. Cornillie, "Combining chromatographic, rheological, and mechanical analysis to study the manufacturing potential of acrylic blends into polyacrylic casts," Materials **14**, 6939 (2021).

[11] Ricarte, R. G., and S. Shanbhag, "A tutorial review of linear rheology for polymer chemists: Basics and best practices for covalent adaptable networks," Polym. Chem. **15**, 815–846 (2024).

[12] Plazek, D. J., and I. Echeverria, "Don't cry for me Charlie Brown, or with compliance comes comprehension," J. Rheol. **44**, 831–841 (2000).

[13] Ricarte, R. G., and S. Shanbhag, "Unentangled vitrimer melts: Interplay between chain relaxation and cross-link exchange controls linear rheology," Macromolecules **54**, 3304–3320 (2021).

[14] Ricarte, R. G., S. Shanbhag, D. Ezzeddine, D. Barzycki, and K. Fay, "Time-temperature superposition of polybutadiene vitrimers," Macromolecules **56**, 6806–6817 (2023).

[15] Baker, C. T., "A perspective on the numerical treatment of Volterra equations," J. Comput. Appl. Math. **125**, 217–249 (2000).

[16] de L. Kronig, R., "On the theory of dispersion of X-rays," J. Opt. Soc. Am. **12**, 547–557 (1926).

[17] Kramers, H. A., "La diffusion de la lumiere par les atomes," Atti Cong. Intern. Fisica, Como **2**, 545–557 .

[18] Rouleau, L., J.-F. Deü, A. Legay, and F. Le Lay, "Application of Kramers-Kronig relations to time-temperature superposition for viscoelastic materials," Mech. Mater. **65**, 66–75 (2013).

[19] Gupta, R., B. Baldewa, and Y. M. Joshi, "Time temperature superposition in soft glassy materials," Soft Matter **8**, 4171–4176 (2012).

[20] Shukla, A., S. Shanbhag, and Y. M. Joshi, "Analysis of linear viscoelasticity of aging soft glasses," J. Rheol. **64**, 1197–1207 (2020).

[21] Winter, H. H., "Analysis of dynamic mechanical data: Inversion into a relaxation time spectrum and consistency check," J. Non-Newtonian Fluid Mech. **68**, 225–239 (1997).

[22] Poudel, S., and S. Shanbhag, "Efficient test to evaluate the consistency of elastic and viscous moduli with Kramers–Kronig relations," Korea-Aust. Rheol. J. **34**, 369–379 (2022).

[23] Shanbhag, S., and Y. M. Joshi, "Kramers-Kronig relations for nonlinear rheology. Part II: Validation of medium amplitude oscillatory shear (MAOS) measurements," J. Rheol. **66**, 925–936 (2022).

[24] Shanbhag, S., and Y. M. Joshi, "Kramers-Kronig relations for nonlinear rheology. Part I: General expression and implications," J. Rheol. **66**, 973–982 (2022).

[25] Hopkins, I. L., and R. W. Hamming, "On creep and relaxation," J. Appl. Phys. **28**, 906–909 (1957).

[26] Knoff, W. F., and I. L. Hopkins, "An improved numerical interconversion for creep compliance and relaxation modulus," J. Appl. Polym. Sci. **16**, 2963–2972 (1972).

[27] Linz, P., *Analytical and Numerical Methods for Volterra Equations* (SIAM, Philadelphia, 1985).

[28] Nikonov, A., A. R. Davies, and I. Emri, "The determination of creep and relaxation functions from a single experiment," J. Rheol. **49**, 1193–1211 (2005).

[29] Sorvari, J., and M. Malinen, "Numerical interconversion between linear viscoelastic material functions with regularization," Int. J. Solids Struct. **44**, 1291–1303 (2007).

[30] Evans, R. M. L., M. Tassieri, D. Auhl, and T. A. Waigh, “Direct conversion of rheological compliance measurements into storage and loss moduli,” Phys. Rev. E **80**, 012501 (2009).

[31] Tassieri, M., R. M. L. Evans, R. L. Warren, N. J. Bailey, and J. M. Cooper, “Microrheology with optical tweezers: Data analysis,” New J. Phys. **14**, 115032 (2012).

[32] Gross, B., *Mathematical Structure of the Theories of Viscoelasticity* (Hermann, Paris, 1953).

[33] Baumgaertel, M., and H. H. Winter, “Determination of discrete relaxation and retardation time spectra from dynamic mechanical data,” Rheol. Acta **28**, 511–519 (1989).

[34] Sorvari, J., and M. Malinen, “On the direct estimation of creep and relaxation functions,” Mech. Time-Depend. Mater. **11**, 143–157 (2007).

[35] Mead, D. W., “Numerical interconversion of linear viscoelastic material functions,” J. Rheol. **38**, 1769–1795 (1994).

[36] Park, S., and R. Schapery, “Methods of interconversion between linear viscoelastic material functions. Part I - a numerical method based on Prony series,” Int. J. Solids Struct. **36**, 1653–1675 (1999).

[37] Luk-Cyr, J., T. Crochon, C. Li, and M. Lévesque, “Interconversion of linearly viscoelastic material functions expressed as Prony series: A closure,” Mech. Time-Depend. Mater. **17**, 53–82 (2013).

[38] Liu, Y., “A direct method for obtaining discrete relaxation spectra from creep data,” Rheol. Acta **40**, 256–260 (2001).

[39] Dooling, P. J., C. P. Buckley, and S. Hinduja, “An intermediate model method for obtaining a discrete relaxation spectrum from creep data,” Rheol. Acta **36**, 472–482 (1997).

[40] Loy, R. J., F. R. de Hoog, and R. S. Anderssen, “Interconversion of Prony series for relaxation and creep,” J. Rheol. **59**, 1261–1270 (2015).

[41] Shanbhag, S., “A computer program for interconversion between creep compliance and stress relaxation,” J. Rheol. **67**, 965–975 (2023).

[42] Kress, R., *Linear Integral Equations*, Applied Mathematical Sciences (Springer, New York, 2013).

[43] Wiff, D. R., “RQP method of inferring a mechanical relaxation spectrum,” J. Rheol. **22**, 589–597 (1978).

[44] Cho, K. S., *Viscoelasticity of Polymers: Theory and Numerical Algorithms* (Springer, Dordrecht, the Netherlands, 2016).

[45] Fuoss, R. M., and J. G. Kirkwood, “Electrical properties of solids. VIII. Dipole moments in polyvinyl chloride-diphenyl systems,” J. Am. Chem. Soc. **63**, 385–394 (1941).

[46] Malkin, A. Y., and I. Masalova, “From dynamic modulus via different relaxation spectra to relaxation and creep functions,” Rheol. Acta **40**, 261–271 (2001).

[47] Larson, R. G., *Constitutive Equations for Polymer Melts and Solutions* (Butterworth-Heinemann, Stoneham, MA, 1988).

[48] Provencher, S. W., “An eigenfunction expansion method for the analysis of exponential decay curves,” J. Chem. Phys. **64**, 2772–2777 (1976).

[49] Takeh, A., and S. Shanbhag, “A computer program to extract the continuous and discrete relaxation spectra from dynamic viscoelastic measurements,” Appl. Rheol. **23**, 24628 (2013).

[50] Shanbhag, S., “pyReSpect: A computer program to extract discrete and continuous spectra from stress relaxation experiments,” Macromol. Theory Simul. **8**, 1900005 (2019).

[51] Shanbhag, S., “Relaxation spectra using nonlinear Tikhonov regularization with a Bayesian criterion,” Rheol. Acta **59**, 509–520 (2020).

[52] Provencher, S. W., “CONTIN: A general purpose constrained regularization program for inverting noisy linear algebraic and integral equations,” Comp. Phys. Comm. **27**, 229–242 (1982).

[53] Honerkamp, J., and J. Weese, “Determination of the relaxation spectrum by a regularization method,” Macromolecules **22**, 4372–4377 (1989).

[54] Weese, J., “A reliable and fast method for the solution of Fredholm integral equations of the first kind based on Tikhonov regularization,” Comp. Phys. Comm. **69**, 99–111 (1992).

[55] Honerkamp, J., and J. Weese, “A nonlinear regularization method for the calculation of relaxation spectra,” Rheol. Acta **32**, 65–73 (1993).

[56] Weese, J., “A regularization method for nonlinear ill-posed problems,” Comp. Phys. Comm. **77**, 429–440 (1993).

[57] Roths, T., M. Marth, J. Weese, and J. Honerkamp, “A generalized regularization method for nonlinear ill-posed problems enhanced for nonlinear regularization terms,” Comp. Phys. Comm. **139**, 279–296 (2001).

[58] Hansen, S., “Estimation of the relaxation spectrum from dynamic experiments using Bayesian analysis and a new regularization constraint,” Rheol. Acta **47**, 169–178 (2008).

[59] Anderssen, R. S., A. R. Davies, and F. R. de Hoog, “On the Volterra integral equation relating creep and relaxation,” Inverse Prob. **24**, 035009 (2008).

[60] Anderssen, R. S., A. R. Davies, and F. R. de Hoog, “On the sensitivity of interconversion between relaxation and creep,” Rheol. Acta **47**, 159–167 (2008).

[61] Anderssen, R. S., A. R. Davies, and F. R. de Hoog, “On the interconversion integral equation for relaxation and creep,” ANZIAM J. **48**, C346–C363 (2007).

[62] Striegel, A. M., “Specific refractive index increment $(\partial n/\partial c)$ of polymers at 660 nm and 690 nm,” Chromatographia **80**, 989–996 (2017).

[63] Kikuchi, M., M. Kobayashi, A. Tanaka, and A. Takahara, “Chain dimension of polystyrene-like hyperbranched polymers with various chain end groups in THF,” J. Phys. Conf. Ser. **184**, 012033 (2009).

[64] Branch, M. A., T. F. Coleman, and Y. Li, “A subspace, interior, and conjugate gradient method for large-scale bound-constrained minimization problems,” SIAM J. Sci. Comput. **21**, 1–23 (1999).

[65] Virtanen, P., R. Gommers, T. E. Oliphant, M. Haberland, T. Reddy, D. Cournapeau, E. Burovski, P. Peterson, W. Weckesser, J. Bright, S. J. van der Walt, M. Brett, J. Wilson, K. J. Millman, N. Mayorov, A. R. J. Nelson, E. Jones, R. Kern, E. Larson, C. J. Carey, İ. Polat, Y. Feng, E. W. Moore, J. VanderPlas, D. Laxalde, J. Perktold, R. Cimrman, I. Henriksen, E. A. Quintero, C. R. Harris, A. M. Archibald, A. H. Ribeiro, F. Pedregosa, P. van Mulbregt, and SciPy 1.0 Contributors, “SciPy 1.0: Fundamental algorithms for scientific computing in python,” Nat. Methods **17**, 261–272 (2020).

[66] Bae, J., and K. S. Cho, “A systematic approximation of discrete relaxation time spectrum from the continuous spectrum,” J. Non-Newtonian Fluid Mech. **235**, 64–75 (2016).

[67] Davies, A. R., and R. S. Anderssen, “Sampling localization in determining the relaxation spectrum,” J. Non-Newton. Fluid Mech. **73**, 163–179 (1997).